Casimir self-assembly: A platform for measuring nanoscale surface interactions in liquids

Citation for the original published paper (version of record):
Hosková, M., Kotov, O., Kücüköz, B. et al (2025). Casimir self-assembly: A platform for measuring nanoscale surface interactions in liquids. Proceedings of the National Academy of Sciences of the United States of America, 122(31): e2505144122-. http://dx.doi.org/10.1073/pnas.2505144122

PNAS RESEARCH ARTICLE | PHYSICS OPEN ACCESS

Casimir self-assembly: A platform for measuring nanoscale surface interactions in liquids

Michaela Hošková[a,b], Oleg V. Kotov[a], Betül Küçüköz[a], Catherine J. Murphy[c], and Timur O. Shegai[a,1]

Affiliations are included on p. 8.

Edited by George Schatz, Northwestern University, Evanston, IL; received March 5, 2025; accepted June 25, 2025

Self-assembly (SA) plays a pivotal role in nanotechnology, offering cost-effective methods for bottom–up fabrication and providing versatile model systems for investigating fundamental interactions in various bioinspired systems. However, current methods for investigating and quantifying the dynamics of SA systems are limited in their applicability to planar interfaces, particularly in liquid environments. These methods typically rely on analyzing the collective behavior of particle suspensions rather than directly probing the specific interactions between individual particles. Here, we introduce Casimir self-assembly (CaSA) as a platform, integrating colloidal science, nanophotonics, and fluctuational electrodynamics to study long-range interactions and stability in planar SA systems. Using thermal fluctuations as a probe and visible-range Fabry–Pérot resonances as an optical readout, we demonstrate that CaSA enables a direct in situ study of the Casimir–Lifshitz electrostatic interaction. This approach allows us to map stability regimes of colloidal materials by varying ionic strength and identifying conditions for stable assembly and aggregation limits, and moreover is used to measure the surface charge density of an individual colloidal object down to fractions of an electron charge per square nanometer. Our platform overcomes the limitations of current methods, providing an experimental tool for exploring SA dynamics in situ and expanding the understanding of suspension stability in liquids at the single-particle level. With potential for future applications, CaSA is scalable for studying interfacial forces and is adaptable to multivalent electrolytes and biosensing.

Casimir effect | self-assembly | optical microcavities | thermal fluctuations | interaction potential

Self-assembly (SA) is a fundamental phenomenon observed on all scales, from atomic and molecular interactions to the formation of galaxies (1). SA is driven by a balance of attractive and repulsive forces. Understanding this balance is essential for controlling SA across diverse systems, with potential applications ranging from biological and nanoscale structures to self-organized colloidal devices (2, 3). The forces driving SA depend on the scale, environment, and types of building blocks involved. Although classical DLVO theory (named after Derjaguin, Landau, Verwey, and Overbeek) describes stability in colloidal systems as an interplay of van der Waals attraction and screened electrostatic repulsion (4, 5), these forces exhibit distinct regimes based on separation distances. At separations of ∼1 nm, quantum electrodynamic dispersion forces manifest as van der Waals interactions in the nonretarded regime. For separations exceeding 100 nm, such as planar interfaces in the presented system, these forces transition to Casimir–Lifshitz interactions in the fully retarded regime (6).

In liquid-based systems, Casimir self-assembly (CaSA) provides a platform for exploring long-range interactions and stability at the nanoscale. Micron-sized gold flakes suspended in ionic solutions spontaneously form Fabry–Pérot (FP) cavities with tunable separation distances of 100 to 200 nm (7) (Fig. 1*A*). This process is governed by a Casimir–Lifshitz electrostatic (CLE) potential (Fig. 1*B*), arising from the balance between attractive Casimir–Lifshitz forces and repulsive screened electrostatic forces. This balance allows for precise control over cavity separations, making CaSA an effective platform for investigating nanoscale interactions and stability in liquid environments (8–11). Moreover, recent research has shown that CaSA can significantly advance the fabrication of photonic structures, mainly the Casimir–Lifshitz optical resonators, which have attracted considerable interest in both theoretical and applied physics (12). The main advantage of this liquid-based SA approach is the potential for active control through external means, such as electric fields (9), radiation pressure (7), or photochemistry (13). Additionally, the FP effect allows for a facile optical readout that enables direct and dynamic measurement of separation distances $L(t)$, which is crucial for accurate quantification of interactions in situ.

Significance

From the natural formation of membranes to the design of advanced materials, self-assembly is fundamental to both living and nonliving systems. However, understanding the forces governing these dynamics, particularly at planar interfaces, remains challenging. Traditional methods often rely on ensemble-averaged measurements, limiting insights into single-particle interactions. To address this, we introduce Casimir self-assembly (CaSA) as a platform that utilizes thermal fluctuations to study the interaction potential in situ. This approach provides precise measurements of zeta potential and surface charge density, key factors in colloidal stability. CaSA overcomes limitations of ensemble methods, offering insight into self-assembly forces. Its sensitivity to ionic conditions enables detection of concentration changes, relevant for sensing, and its responsiveness opens possibilities for feedback-controlled microfluidic systems.

The authors declare no competing interest.

This article is a PNAS Direct Submission.

[1]To whom correspondence may be addressed. Email: timurs@chalmers.se.

This article contains supporting information online at https://www.pnas.org/lookup/suppl/doi:10.1073/pnas.2505144122/-/DCSupplemental.

Published August 1, 2025.

The Casimir force, a sizable effect arising from quantum field fluctuations, was first predicted by H. B. Casimir in 1948 as an attractive force acting between two uncharged, perfectly conducting plates in a vacuum (14). Later, E. M. Lifshitz and coworkers generalized this force to include real material properties and media, leading to the Casimir–Lifshitz theory (15, 16). The Casimir effect has been extensively explored in contexts such as quantum torque and nanoalignment (17–19), oscillators (20), repulsion (21–23), levitation (24), atomic-scale interactions (25), advanced nanodevices (26, 27), and interactions in biological systems (28). Despite these advances, direct measurements of Casimir–Lifshitz forces in plane-parallel configurations remain rare (29–31). In addition to the Casimir–Lifshitz force, equally charged objects in liquid solutions experience a counteracting screened electrostatic repulsion due to electric double-layer formation. These interactions are governed by the Debye–Hückel screening length (κ^{-1}), which depends on the ionic strength (I) of the solution and plays a crucial role in balancing attractive and repulsive forces (6). At separation distances of approximately 100 nm, these two forces remain the only significant interactions, as other interparticle forces become negligible. Although the gravitational force is still present, it contributes less than 1% of the Casimir force. The zeta potential (ζ), representing the electrostatic potential at the slipping plane, is a key parameter that directly influences the stability of such systems. By adjusting the ionic strength, one can modulate the double-layer thickness (κ^{-1}) and the ζ-potential, thereby achieving precise control over both stability and tunability. However, understanding and accurately measuring the ζ-potential remains challenging. Electrophoretic methods, which dominate the ζ-potential measurements, rely on simplifying assumptions that often limit their accuracy, particularly under low ionic strength conditions (32, 33). Furthermore, most existing methods are based on ensemble-level analyses, which average over multiple particles, and therefore, single-particle measurements remain challenging.

In this study, we present an optical approach to in situ probing of CLE interactions in liquid-based SA systems, in the plane-parallel configuration as presented in the original Casimir force theory. Our experiments, conducted in a monovalent electrolyte surfactant-salt solution, align well with theoretical predictions from the Lifshitz theory of Casimir forces and with the Gouy–Chapman model of the electric double-layer. By leveraging thermal fluctuations and visible-range FP resonances, we analyze long-range CLE interactions and reconstruct the interaction potential under varying ionic strength and micron-size interaction areas. This approach enables precise mapping of CaSA stability regimes and identifies aggregation mechanisms, focusing on individual micron-sized planar flakes rather than collective suspension behavior. Importantly, our approach allows to introduce a method for measuring the surface charge density σ and ζ-potential of planar flakes at a single-particle level. This expands the utility of the CaSA platform as a powerful tool for understanding SA dynamics at the single-particle level with potential applications in sensing, microfluidics, and other fields requiring precise control over liquid-based system stability.

Results

System Under Study and Measurement of Thermal Fluctuations. Fig. 1*A* illustrates the Casimir self-assembled optical microcavity composed of two gold flakes formed in a surfactant-salt solution. This system consists of an upper floating flake, synthesized through a rapid, seedless wet chemical method (34), and a static bottom flake, represented by a 20 nm gold layer deposited on a glass substrate (with a 2 nm chromium adhesion layer) and nanopatterned using electron beam lithography. The semitransparent floating flakes, typically ~30 nm thin, were selected and positioned using the optical tweezers method to match the dimensions of the bottom flake. We used the bottom nanopatterned layer approach, demonstrated in previous studies (18), to determine the size of the upper floating flake and to minimize lateral Brownian motion in liquid. All samples were prepared in a controlled, sealed chamber, as detailed in the methods section. This setup minimized environmental factors, such as evaporation, temperature, and concentration gradients, and prevented hydrodynamic forces from impacting the SA process. We maintained the surfactant concentration (CTAB, cetyltrimethylammonium bromide) at 0.05 mM, well below the critical micelle concentration (CMC), to avoid depletion forces and prevent micelle formation. We systematically varied the ionic strength of the solution by adjusting the ionic strength of potassium bromide (KBr) from 0.1 mM to 1 mM to investigate its effects on stability and tunability. Bromide ions (Br^-) are known to reduce electrostatic repulsion on positively charged gold surfaces, which enhances the adsorption of CTAB molecules in a synergistic manner, as observed in similar systems (35). We measured datasets capturing changes in $L(t)$ between bottom and floating flakes (fluctuations) under various conditions (Fig. 2). To evaluate whether these fluctuations reflect the real shape of the interaction potential governing SA, we collected the reflectivity spectra over time and analyzed selected FP resonances $\lambda_{FP}(t)$ using the transfer matrix method (TMM) to extract precise separation distances (Fig. 2*A*). By fitting these data, we derived a calibration curve that relates $\lambda_{FP}(t)$ to $L(t)$, which was then applied to the full dataset (*SI Appendix*, Fig. S1).

Influence of Ionic Strength and Interaction Surface Area on Thermal Fluctuations of Floating Flakes. To determine whether thermal fluctuations reflect concentration changes in the liquid solution, we first analyzed cavities of similar interaction areas (approximately $25 \pm 5\,\mu m^2$) formed in solutions of different ionic strengths (Fig. 2*B*). Time-resolved reflectivity spectra were recorded with a time step of $\Delta t = 0.015$ s, corresponding to the camera's cycle time. Each data point was acquired with an exposure time of 0.01 s. The normalized histograms represent experimental probability distribution functions (PDFs) of the flake's position at various separation distances and were compared to theoretical PDFs calculated from Boltzmann distributions using the calculated interaction potentials. The experimental PDFs were computed using the standard definition, PDF $= n_i/(N\Delta L)$, where n_i is the number of measured separations within ith bin, N is the total number of measurements, and ΔL is the bin width. This yields a properly normalized PDF with units of inverse length. Two key parameters were determined from the measured data: the equilibrium separation distance (L_{eq}) and the fluctuation amplitude, derived as the SD of the separation distances.

We observed that concentrated solutions (dark red) form stable cavities with L_{eq} around 93 nm and minimal SDs (±1 nm), while diluted solutions (yellow) form less stable cavities with L_{eq} closer to 193 nm and larger deviations (±5 nm). Intermediate concentrations show a transition between these extremes.

To complement our analysis of the effects of ionic strength in a monovalent ionic solution, we further investigated how the size of the interaction area influences stability within the CaSA cavities. Specifically, we examined cavities with interaction areas ranging

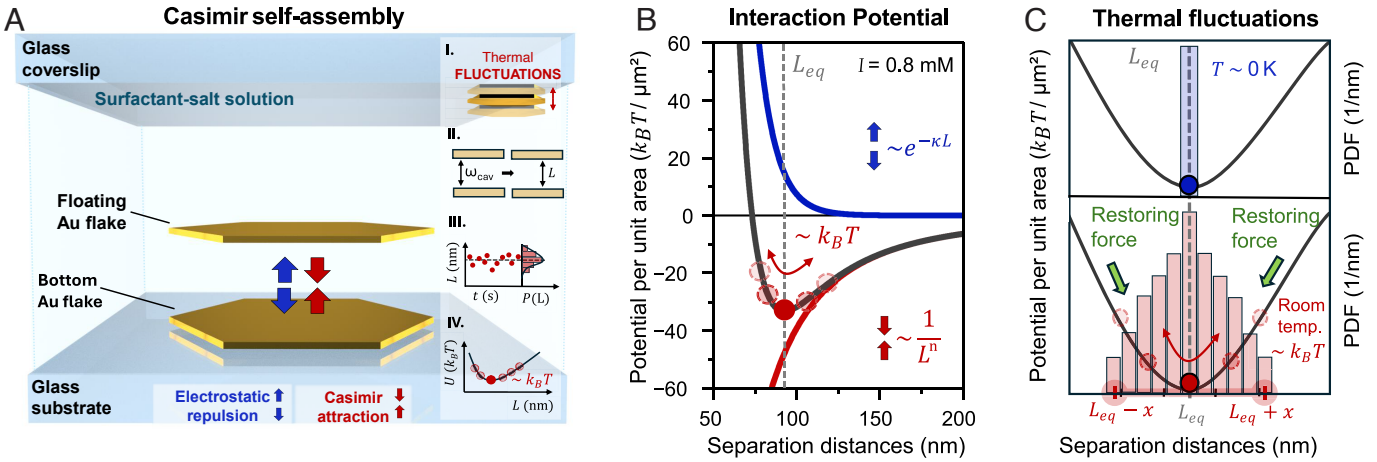

Fig. 1. (*A*) Schematic representation of the CaSA system under study, composed of two gold flakes: the upper floating flake and the bottom static flake. The right column (I–IV) illustrates the main concept of studying how thermal fluctuations provide experimental insight into the system's interaction potential: I) thermal fluctuations of the upper floating flake, II) measurement of separation distances, III) statistical analysis, IV. potential reconstruction. (*B*) Calculated CLE potential, showing the balance between the long-range attractive Casimir–Lifshitz force and the screened electrostatic repulsion. (*C*) Analogy of thermally driven fluctuations in CaSA systems, described as a particle trapped in a potential well. At near-zero temperature, the particle remains in the potential minimum, while at room temperature, the particle fluctuates around the equilibrium (L_{eq}) because of thermal energy received from the surrounding environment.

from 6 to 42 μm^2 at a fixed ionic strength of 0.3 mM (Fig. 2*C*). We observed that larger interaction areas significantly increased stability, as indicated by the reduced vertical fluctuations around L_{eq} (see *SI Appendix*, Fig. S2 for the detailed dependence of SD on ionic strength and interaction area, along with extracted surface charge density values across different cavity sizes). This finding contrasts with typical challenges in lithography, where decreasing feature sizes often lead to increased uncertainties in precision. However, in our system, increasing the surface area of the interaction led to more stable cavities, resulting in smaller gaps and reduced fluctuations, as reflected in the decrease in SD.

These observations, along with the effects of ionic strength, reflect changes in the interaction potential that govern the SA process. While L_{eq} reflected the position of the CLE potential minimum, the SD provided a measure of the potential width. Cavities formed in concentrated solutions exhibited symmetric distributions, indicating a symmetric, deep, and narrow interaction potential. In contrast, diluted solutions showed slightly asymmetric distributions, corresponding to a shallower and broader potential. This analysis highlights three key properties: symmetry or asymmetry of the interaction potential, the qualitative depth of the potential, and its width, each of which varies with the ionic strength and interaction area.

Casimir–Electrostatic Interaction Potential. To systematically investigate the interaction potential within the CaSA system, we employed both experimental measurements and theoretical modeling. We first reconstructed the CLE interaction potential based on the discrete probability histogram obtained from the measured separations, using $P(L) = n_i/N$, where n_i is the number of measurements falling into ith bin, and N is

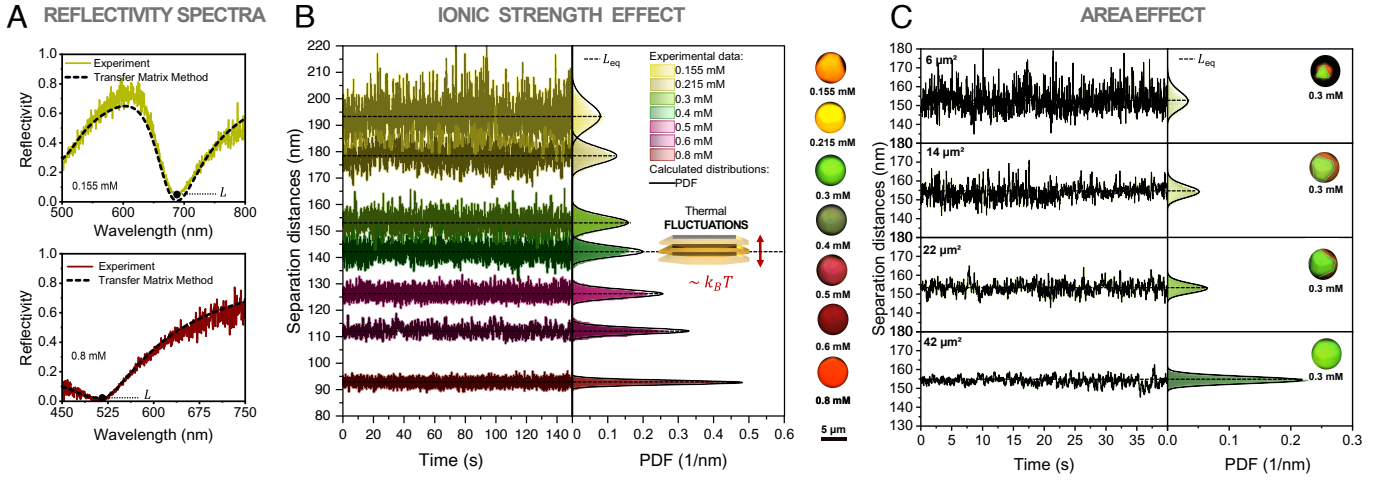

Fig. 2. (*A*) Reflectivity spectra of the formed cavities with Fabry–Pérot resonances fitted using the transfer matrix method to extract information about separation distances (*L*). (*B*) Study of ionic strength effect: reflectivity spectra measured in real-time with a time step $\Delta t = 0.015$ s and exposure time 0.01 s to analyze vertical fluctuations around the equilibrium position (L_{eq}) for various ionic strength (CTAB maintained at 0.05 mM, KBr varied). Normalized histograms representing the measured probability distribution functions (PDFs) of flake positions at different separation distances (*L*), compared to calculated PDF curves. Images of real Casimir self-assembled microcavities formed on top of a gold film are shown to demonstrate their appearance under the microscope at different ionic strengths, where the observed colors indicate specific separation distances. (*C*) Effect of interaction area on stability at a fixed ionic strength (0.3 mM), showing that larger areas result in reducing deviations and enhancing stability at room temperature.

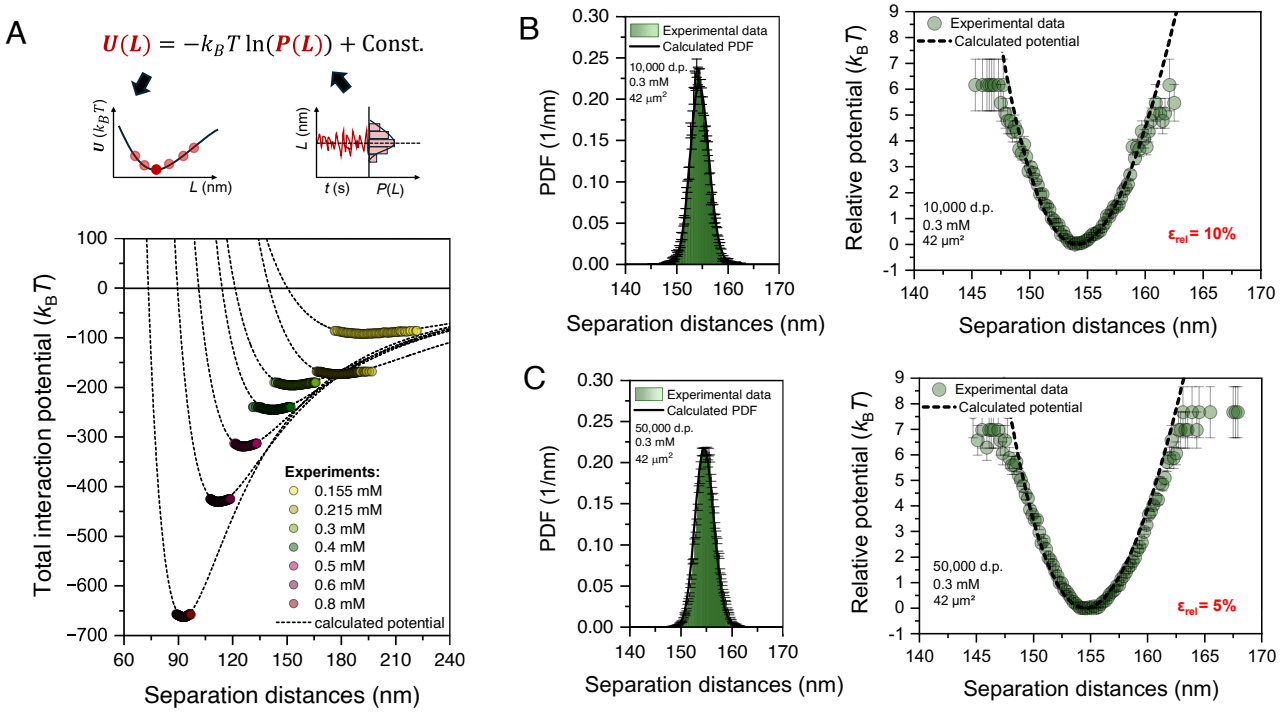

Fig. 3. (*A*) Reconstruction of the total CLE interaction potential of microcavities formed at different ionic strengths. The probability distribution function PDF of separation distances was measured experimentally and is schematically shown as a histogram. The calculated potentials $U(L)$, normalized to the actual cavity interaction area *A*, illustrate how the potential shape evolves with ionic strength. For low ionic strength (0.05 mM), the potential is shallow and broad (see the dashed rainbow line in *SI Appendix*, Fig. S3*A*), leading to unstable configurations. At intermediate ionic strengths (0.155 to 0.8 mM), the potential becomes deeper, narrower, and more symmetric, resulting in stable equilibrium configurations. At high ionic strength (~2 mM), attractive forces dominate, leading to aggregation (dashed gray line, *SI Appendix*, Fig, S3*A*). (*B*) Experimentally obtained relative CLE potential (green dots with experimental errorbars) at 0.3 mM ionic strength, reconstructed from 10,000 data points (cavity size 42 μm^2). Comparison with the theoretically calculated curve shows a reasonable agreement, capturing the shape of the potential and the equilibrium position ($\varepsilon_{rel} = 10\%$). Measured histograms for the separation distances are also shown. (*C*) Improved accuracy in the reconstruction of the CLE potential achieved by collection of 50,000 data points by increasing collection time for a 42 μm^2 cavity formed at 0.3 mM ionic strength. The experimental data are in close agreement with the theoretically calculated potential ($\varepsilon_{rel} = 5\%$), highlighting the importance of extended data collection to reduce uncertainties.

the total number of recorded measurements. This allowed us to directly compare the experimentally reconstructed potential with the theoretical model, assessing the agreement between measured and predicted interactions. Furthermore, this approach enabled us to evaluate whether thermal fluctuations could serve as a probe for the interaction forces present within the system.

Using Boltzmann distribution principles, we extracted the relative interaction potential $\Delta U(L)$ of individual cavities from the measured probability histogram of flake separation distances. The reconstruction equation is given by

$$\Delta U(L) = -k_B T \ln(P(L)) + C, \qquad [1]$$

where k_B is the Boltzmann constant, T is the temperature, $P(L)$ is the probability of finding the system at a separation distance L, and C is a normalization constant. The reconstructed potential $\Delta U(L)$ represents the interaction energy relative to its minimum at the equilibrium separation L_{eq}, such that $\Delta U(L) = U(L) - U(L_{eq})$. It is important to note that the reconstructed $\Delta U(L)$ reflects the total interaction energy corresponding to the actual interaction area of the cavity, rather than showing values normalized per unit area.

In Fig. 3*A*, we compare the experimentally reconstructed CLE potential with the calculated potential (theoretical calculations detailed in *Methods*). The experimental potential, represented as a relative potential, was shifted along the *y*-axis by a constant D (corresponding to the depth of theoretical potential) to align with the calculated curve. The values of this constant are provided in *SI Appendix*, Fig. S3*B*. The comparison emphasizes agreement in key aspects such as the position of the minimum (L_{eq}), the shape, and the width of the potential, rather than its absolute depth. The calculated curves indicate that at low ionic strength (0.05 mM), the interaction potential is shallow, with a minimum of approximately $3\,k_B T$ per μm^2, resulting in an unstable configuration where flakes can tilt freely (dashed rainbow line, *SI Appendix*, Fig. S3*A*). As the ionic strength increases, the interaction potential deepens and becomes narrower and more symmetric, reaching a minimum of up to $25\,k_B T$ per μm^2 in stable configurations. At higher ionic strength (2 mM), attractive forces dominate, leading to gold flakes aggregation, i.e., $L_{eq} \to 0$ (dashed gray line, *SI Appendix*, Fig. S3*A*). Fig. 3 *B* and *C* provides a detailed reconstruction of the interaction potential at an ionic strength of 0.3 mM, illustrating the PDFs alongside the relative potential. To evaluate the influence of data collection time on the accuracy of the potential reconstruction, we compared reconstruction from two datasets measured at the same ionic strength (0.3 mM) and interaction area (42 μm^2), containing 10,000 and 50,000 data points, respectively. As shown in Fig. 3 *B* and *C*, the potential reconstructed from the longer dataset (12.5 min) exhibits a closer match to the theoretical curve. To quantify this difference, we calculated the relative error ε_{rel}, defined as the normalized deviation between the experimental and calculated stiffness. The shorter dataset yields $\varepsilon_{rel} = 10\%$, whereas the longer dataset achieves $\varepsilon_{rel} = 5\%$, indicating improved accuracy with increased data points.

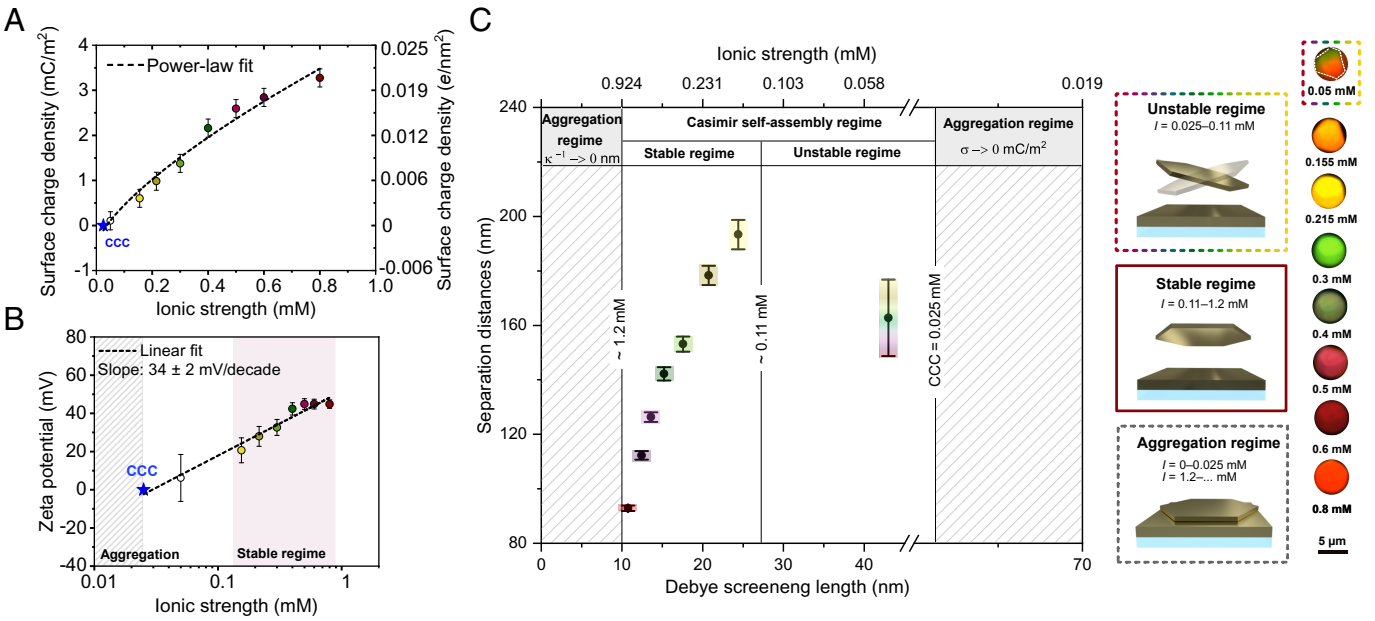

Fig. 4. (*A*) Surface charge density (σ) as a function of ionic strength, fitted with a power-law function. The data highlight the nonlinear dependence of σ on ionic strength. Error bars represent propagated uncertainties in σ derived from the measurements of separation distance with precision ±4 nm, determined using the transfer matrix method (TMM). (*B*) Zeta potential (ζ) plotted as a function of ionic strength on a logarithmic scale, showing a clear linear relationship in the lin–log representation. A linear fit of the data yields a slope of 34 ± 2 mV/decade. (*C*) Working range and stability limits of Casimir self-assembled cavities studied by ionic strength variation. The figure shows the regimes of aggregation and CaSA, determined by the balance of Casimir–Lifshitz attraction and screened electrostatic repulsion. Aggregation occurs in both diluted and concentrated solutions, characterized by strong attraction without a local potential minimum. Within the CaSA regime (0.155 to 0.8 mM), equilibrium separation distances decrease with increasing ionic strength, reflecting stronger confinement. Unstable cavities exhibit shallow and broad interaction potentials, while stable cavities show narrow and deeper potentials. Side images illustrate these behaviors across the aggregation and assembly regimes. The last column presents real Casimir self-assembled microcavities formed on top of a gold film, with Fabry–Pérot resonance colors corresponding to different separation distances.

A complete overview of reconstructed interaction potentials for all measured cavities, together with the corresponding relative errors ε_{rel}, is presented in *SI Appendix*, Fig. S4). The same section (*Flake Dynamics and Single-Particle Tracking*) also details the extraction of key dynamic parameters, including the relaxation time, stiffness, and diffusion coefficient, from single-particle trajectories (*SI Appendix*, Figs. S4–S8). A full explanation of error determination, including its derivation and propagation, is provided in *SI Appendix*, section 3.

Zeta Potential and Stability of Self-Assembled Microcavities. To investigate the balance between screened electrostatic repulsion and Casimir–Lifshitz attraction and their effects on the stability of self-assembled microcavities, we analyzed statistically processed data from the fluctuations of individual flakes $L(t)$ across different ionic strengths (Fig. 2 *B* and *C*). By focusing on the system properties at equilibrium (L_{eq}), we were able to extract and measure the surface charge density σ and ζ-potential at the single-particle level.

The surface charge density σ of the upper floating flake was determined by applying the equilibrium condition:

$$\left.\frac{dU(L, I, \sigma)}{dL}\right|_{L_{\text{eq}}} = 0. \qquad [2]$$

Solving this equation allowed us to extract σ for the given ionic strength I. Using this condition, we extracted σ for each system (Fig. 4*A*). We further established a relationship between the extracted surface charge density (σ) and the electrokinetic charge density (σ_e), which corresponds to the ζ-potential, by applying the Gouy–Chapman model of the electric double layer. In monovalent electrolytes with ionic strengths below 1 mM, the surface potential (ψ_0), diffuse layer potential (ψ_d), and ζ-potential can be considered approximately equal ($\psi_0 \approx \psi_d \approx \zeta$), as confirmed by experimental and theoretical studies (36–41). Using the Grahame equation (42), we quantified the relationship between σ_e and ζ-potential:

$$\sigma \approx \sigma_e = \sqrt{8 c_0 \varepsilon \varepsilon_0 k_B T}\, \sinh\left(\frac{ze\zeta}{2k_B T}\right), \qquad [3]$$

where c_0 is the bulk concentration of the salt (which is equivalent to the ionic strength for monovalent salt), ε is the static permittivity of the water solution, ε_0 is the vacuum permittivity, z is the ion valence, and e is the elementary charge.

Our results, presented in Fig. 4 *A* and *B*, demonstrate a strong dependence of both σ and ζ-potential on ionic strength I. As shown in Fig. 4*A*, σ exhibits a nonlinear increase with I, which we fitted using a power-law function, $\sigma(I) = -0.44 + 4.6\, I^{0.7}$. The base value of σ corresponds to $-0.44 \pm 0.3\ \text{mC/m}^2$, representing the surface charge density in solution under conditions of negligible screening due to low ionic strength (43). However, for instance, at an ionic strength of 0.3 mM, increased screening led to a measured surface charge density of $1.38\ \text{mC/m}^2$.

Fig. 4*B* presents the ζ-potential as a function of ionic strength on a logarithmic scale (obtained from the Grahame equation [**3**]), revealing a clear linear trend in the lin–log representation. For comparison, the same data are plotted in a lin–lin scale in *SI Appendix*, Fig. S10, providing an alternative visualization of the ζ-potential dependence on ionic strength. The data were fitted with a linear model, yielding a slope of 34 ± 2 mV/decade. For instance, at an ionic strength of 0.3 mM, the measured ζ-potential was at approximately 33 mV, a value commonly associated with stable suspensions, in agreement with the stability

observed in our experiments. The critical coagulation concentration (CCC) was observed at an ionic strength of 0.025 mM, where both the ζ-potential and surface charge density (σ) approach zero, marking the transition from stable SA to aggregation. Error bars represent propagated uncertainties from the measured separation distances (L), determined with a precision of ± 4 nm using TMM. As detailed in *SI Appendix*, section 3, these uncertainties account for flake thickness and material dispersion. No error bars are assigned to the CCC, as this concentration was determined through visual observations of flake aggregation rather than direct quantitative measurements. This is due to the absence of thermal fluctuations at CCC, where interparticle repulsion vanishes, leading to irreversible aggregation.

Furthermore, we identified three distinct stability regimes within the CaSA system: aggregation, unstable, and stable. In the aggregation regime, which occurs at either relatively low (<0.025 mM) or high (>1.2 mM) ionic strengths, the interaction potential lacks a local minimum (except for a trivial $L_{eq} \rightarrow 0$ condition). At low ionic strengths below the CCC, weak electrostatic repulsion was insufficient to counteract Casimir–Lifshitz attraction, leading to aggregation. Conversely, at high ionic strengths, where the Debye screening length (κ^{-1}) becomes shorter than 1 nm, the Casimir attraction dominated, driving aggregation. Within the CaSA regime (100 to 200 nm), the formation of cavities is driven by CLE potentials due to the presence of a local minimum. As ionic strength increases, the equilibrium separation distance L_{eq} is observed to decrease from 193 nm to 93 nm. Additionally, cavity stability improved with increasing ionic strength, as indicated by a decrease in SD from 5 nm to 1 nm. This trend, represented by the color-coded bars in Fig. 4*C*, corresponds to the narrowing of the CLE potential. The unstable regime (0.025 to 0.11 mM) was characterized by observing multiple FP modes attributed to flake tilting. This instability resulted from a shallow and broad interaction potential, as illustrated by the dashed rainbow line in *SI Appendix*, Fig. S3*A*.

Discussion

In this work, we introduce the CaSA as a platform for measuring nanoscale surface interactions and investigating SA dynamics in liquids. By utilizing thermal fluctuations as a probe and FP resonances as an optical readout, we explored various properties at a single-particle level. We reconstructed the CLE interaction potential, analyzed the surface charge density σ and ζ-potential, and mapped stability regimes and aggregation behavior under different ionic conditions.

Measurement of CLE Interaction Potential In Situ. We addressed the challenges of in situ measurement of the CLE potential between planar surfaces, crucial for understanding the forces governing SA in liquids. By analyzing the thermal fluctuations of the upper floating flakes, we reconstructed and captured the width, equilibrium position, and shape of the potential across varying ionic strengths and for different interaction areas. Our reconstruction methodology, based on the principles established by Prieve et al. (44), overcomes limitations, where conventional techniques such as single-particle tracking (SPT) (45–47), total internal reflection microscopy (TIRM) (44, 48), surface force apparatus (SFA) (49) and atomic force microscopy (AFM) (50–53) are unsuitable for in situ analysis of interactions between planar surfaces. A detailed comparison between CaSA and these established surface force techniques is provided in *SI Appendix*, section 5.

Our results highlight the influence of data collection time on reconstruction accuracy, confirming that longer collection time improves reconstruction precision. This aligns with the findings of Willemsen et al. (53), as larger datasets reduce statistical errors. In our study, we collected the spectra with a $\Delta t = 0.015$ s over approximately 2.5 min (or 12.5 min for longer measurements), resulting in 10,000 (or 50,000) data points, respectively. This acquisition rate is significantly higher than in previous works, which primarily aimed to demonstrate system dynamics rather than reconstruct the full interaction potential. For instance, Zhao et al. measured FP spectra with a time step of ~30 s and collected 47 data points over 23 min (23), while Munkhbat et al. acquired 39 data points with a time step of 0.026 s (7). In our case, the short time step was selected to remain below the characteristic relaxation time τ_0 of each system (*SI Appendix*, Fig. S5 *C* and *D*), ensuring accurate tracking of upper flake fluctuations $L(t)$. For cavities formed in ionic strengths ranging from 0.1 to 1 mM, the relaxation time lies in the range of 0.017 to 0.3 s, depending on the size of the upper floating flake and the ionic strength. This approach provided sufficient statistical resolution for potential reconstruction and further enabled access to single-particle dynamics, such as autocorrelation function (ACF) and mean squared displacement (MSD) analysis, discussed in *SI Appendix*, section 2.

In summary, the CaSA platform is a complementary method to existing techniques, offering distinct advantages: i) fully in situ operation without mechanical contact, ii) direct access to interaction potentials between planar geometries, iii) simultaneous measurement of dynamic parameters such as diffusion coefficients and characteristic relaxation times, and iv) sensitivity to weak long-range forces with larger flakes, where narrower and deeper potentials lead to stable SA. Current limitations include the need for optically responsive materials with high reflectivity in the visible spectral range and well-defined geometry, as reconstruction relies on the fluctuation statistics of flakes and optical spectrum fitting. In addition, at higher ionic strengths, gold flakes tend to aggregate, which prevents stable cavity formation and limits the platform's applicability under such conditions. This limitation may be overcome by surface functionalization or by using dielectric cavities, where weaker Casimir–Lifshitz forces could still support stable equilibrium even at higher salt concentrations (>10 mM).

Zeta Potential Measurements of Planar Interfaces at the Single-Particle Level. Our study enhances the understanding of suspension stability by extending the classical DLVO theory to include systems of micron-sized particles with larger separation distances (greater than 100 nm). We present in situ measurements of the surface charge density (σ) and the ζ-potential for planar interfaces at the single-particle level.

A comparison with conventional methods for measuring the ζ-potential of nanoscale objects highlights key differences and advantages. The most commonly used technique relies on dynamic light scattering (DLS) with an electrophoretic mobility cell, where an alternating voltage is applied to the colloidal solution. The average ζ-potential is then inferred from the electrophoretic mobility using the Henry equation (54). This approach is widely used for characterizing colloidal stability. However, it provides only an ensemble-averaged value over billions of nanoscale particles, typically ranging from 3 nm to several microns, and is highly sensitive to factors such as ionic strength, pH, and sample concentration (55). Moreover, it does not yield direct information on the surface charge density σ,

a key parameter for understanding electrostatic interactions at the nanoscale. In contrast, our method enables the direct determination of the ζ-potential and surface charge density σ at the single-particle level. By eliminating the need for external electric fields and avoiding the assumptions in electrophoretic techniques, it offers an alternative to conventional ensemble-based methods, which inherently obscure individual particle behavior through averaging.

At an ionic strength of 0.3 mM, we experimentally determined a surface charge density of 1.38 mC/m^2, which, when converted using Graham's equation (6, 39, 41, 56), corresponds to a ζ-potential of approximately 33 mV. This relatively low value indicates a balance between positive and negative charges within the slipping plane ($\sigma_{ek} \approx \sigma$). It is primarily caused by the the asymmetrical distribution of ions within the slipping plane, largely driven by the adsorption of CTA^+ ligands onto the surface. The total positive charge, contributed by both CTA^+ and K^+ ions, exceeds the negative charge from Br^- ions. This imbalance can be expressed as

$$\sigma = |\sigma^+ - \sigma^-| = |(\sigma_{CTA^+} + \sigma_{K^+}) - \sigma_{Br^-}| \neq 0, \quad [4]$$

where σ_{CTA^+} and σ_{K^+} represent the positive charge densities of counterions, and σ_{Br^-} corresponds to the negative charge density from bromide ions. The measured value aligns with those reported for similar systems (57, 58).

The power-law dependence of σ on ionic strength reveals a complex interplay between bromide ion screening and CTA^+ adsorption. At low ionic strength, electrostatic repulsion between CTA^+ headgroups limits adsorption, while increasing ionic strength facilitates bromide ions to mitigate these repulsions and enable denser packing of CTA^+ molecules, as reported by Vivek et al. (35). Chen et al. (43) illustrated a power-law relationship between the ζ-potential and σ as a function of ion concentration for borosilicate particles in monovalent solutions, which supports the nonlinear trends observed in this study.

The CCC, which was observed at an ion concentration of 0.025 mM, indicates a state where both the net surface charge and the zeta potential are close to zero. This equilibrium results in particle aggregation, as evidenced by experimental observation. The measured CCC of 0.025 mM is consistent with concentrations reported in previous studies on CTAB-stabilized colloidal systems (59–62). Similarly, the linear slope of the ζ-potential in the lin–log scale, 34 ± 2 mV/decade, reflects the characteristic response of surfactant-stabilized interfaces to variations in ionic strength. The measured ζ-potential values, ranging from approximately 20 to 45 mV for ionic strengths between 0.1 and 1 mM, are consistent with previously reported data for similar monovalent surfactant-salt systems (63–66). By providing precise measurements of the ζ-potential and σ, the CaSA platform offers potential utility as a model system for exploring specific ionic effects (SIE) and stability in multivalent electrolyte solutions. Furthermore, the platform could be applied in biosensing technologies.

Conclusion

We introduced CaSA as a promising platform for measuring nanoscale surface interactions in liquids. By combining thermal fluctuations as a probe with FP resonances as an optical readout, we achieved direct, in situ measurements of the CLE interaction potential, surface charge density σ, and zeta potential ζ at the single-particle level. This methodology overcomes the limitations of conventional ensemble-based techniques by providing precise insights into planar interface interactions in monovalent electrolyte solutions. Our results expanded the understanding of SA stability regimes, revealing transitions between aggregation, unstable, and stable configurations governed by ionic strength. The reconstructed CLE potential and ζ-potential measurements are consistent with theoretical predictions by Poisson–Boltzmann and Casimir–Lifshitz potentials within the studied parameters and known stability ranges, confirming the accuracy and reliability of the presented approach. Beyond its fundamental significance, the CaSA platform offers unique advantages for practical applications. Presented tunable optical cavities are highly sensitive to changes in ionic strength, surface charges, and ligand adsorption, enabling label-free sensing through shifts in resonance or fluctuation dynamics. Formed directly in liquid, these cavities can be dynamically controlled via external fields, temperature, or chemical gradients, providing a foundation for smart microfluidic systems with real-time optical feedback. This makes CaSA a promising tool for investigating ionic effects in multivalent electrolytes and advancing liquid-based sensing technologies.

Methods

Nanofabrication and Experimental Chamber Setup . All measurements of the formed Casimir self-assembled cavities were performed in an experimental chamber designed to prevent liquid solution evaporation and ensure steady-state conditions without external influences. The chamber consisted of three parts: the bottom coverslip glass (gold-covered and nanopatterned), a polydimethylsiloxane (PDMS) spacer as an O-ring, and an upper coverslip glass as a lid. The 170 μm thin microscope glass coverslips were first cleaned using acetone, 2-propanol, and water in an ultrasonicator at 50 °C for 15 min each. After drying with compressed nitrogen, the coverslips were subjected to oxygen plasma cleaning. A 2 nm Cr layer was evaporated onto the glass substrate to enhance adhesion, followed by a 20 nm Au layer using the Kurt J. Lesker physical vapor deposition (PVD) 225 evaporator. The bottom coverslip glass was further nanopatterned. Gold seed arrays (bottom static flakes) with various edge sizes were fabricated using electron-beam lithography (Raith EBPG 5200). The PDMS O-ring was placed on the bottom static mirror, and 4 μL of gold flakes solution containing 0.05 mM CTAB was drop-casted inside the chamber. The solution was subsequently mixed with 4 μL of KBr salt solution in 0.05 mM CTAB at various ionic strengths, and the chamber was sealed with an upper coverslip glass.

Synthesis of Gold Micron-Sized Flakes and Surfactant-Salt Solution Mixture. Floating gold flakes were synthesized using a seedless wet chemical method, which produces micron-sized gold flakes with lateral dimensions of 1 to 10 μm and a thickness of approximately 25 to 35 nm (34). First, 100 μL of 100 mM $HAuCl_4$ was added to 3 mL of 20 mM CTAB solution and stirred at room temperature. Then, 100 μL of 100 mM ascorbic acid was added, and the mixture was shaken for 30 s and subsequently heated at 85 °C for 1 h. The resulting gold flakes were purified by washing with deionized water and stored in a 20 mM CTAB solution to prevent aggregation (complete CTAB bilayer formed), and then diluted in 0.6 mM CTAB for storage. The final ionic strength was adjusted with an aqueous solution of potassium bromide (KBr). To prepare the KBr solution, KBr salt was dissolved in deionized water to achieve a stock solution of 100 mM. Before each experiment, the stock solution containing gold flakes in 0.6 mM CTAB was diluted with deionized water to obtain a working solution of 0.05 mM CTAB. This diluted solution was drop-cast onto the static gold mirror. To adjust the final ionic strength, an equal volume of a KBr solution in 0.05 mM CTAB was added, ensuring constant CTAB concentration (0.05 mM) across all experiments.

Optical Measurements and Transfer Matrix Method. An inverted microscope (Nikon Eclipse TE2000-E) with an oil immersion 100× objective (switchable NA = 0.5 to 1.3, Nikon) was used for optical reflection spectra

measurements. All measurements were performed using a halogen light source as a bottom illumination, fiber-coupled to the microscope. The time-resolved reflection spectra at normal incidence (NA = 0.5) were collected using the same objective and directed to a fiber-coupled spectrometer (Andor Shamrock SR-500*i*). Fluctuations were measured in the spectrometer's kinetic mode (exposure time = 0.01 s, cycle time = 0.015 s) equipped with a CCD detector (Andor Newton 920). To extract the separation distances, reflection spectra were further analyzed by the standard transfer matrix method and fitted by reflection coefficient at normal incidence calculated assuming 2 nm Cr, 20 nm thin bottom gold flake, 33 nm thin floating flake, solution refractive index $n = 1.33$, and a glass substrate of refractive index $n = 1.51$. In addition, a continuous-wave laser was used for real-time manipulation of flakes in the solution. Specifically, a continuous-wave laser ($\lambda = 447$ nm, 9 mW) was focused through a 100× objective (NA = 1.3). This setup generated an optical trap that attracted gold flakes to the beam, allowing precise positioning relative to the sample and accelerating the formation of microcavities.

CLE Potential Calculation. The total CLE interaction potential per unit area, $u(L)$, was calculated by summing the Casimir–Lifshitz attractive interaction ($u_{\mathrm{CL}}(L)$) and the Poisson–Boltzmann screened electrostatic repulsive interaction ($u_{\mathrm{el}}(L)$):

$$u(L) = u_{\mathrm{CL}}(L) + u_{\mathrm{el}}(L). \quad [5]$$

The Casimir–Lifshitz potential per unit area, $u_{\mathrm{CL}}(L)$, was calculated using Lifshitz theory in the zero-temperature approximation (7, 67):

$$u_{\mathrm{CL}} = \frac{\hbar}{2\pi}\int_0^\infty d\xi \int \frac{d^2\mathbf{k}_\parallel}{(2\pi)^2} \ln\det \mathbf{G}. \quad [6]$$

Here, $\mathbf{k}_\parallel$ represents the in-plane wave vector component, and $\mathbf{G}$ is the reflection operator matrix incorporating material properties through Fresnel reflection coefficients. The permittivity of gold was calculated using the Drude model, and the permittivity of water was described using the Debye–Lorentz model. A detailed derivation, along with a comparison to the finite-temperature approach, is provided in *SI Appendix*, Fig. S11).

The screened electrostatic potential, $u_{\mathrm{el}}(L)$, was calculated in accordance with the Poisson–Boltzmann theory, which describes the electric double-layer repulsion between charged planar interfaces in an electrolyte as (56):

$$u_{\mathrm{el}}(L) = \frac{2\sigma^2}{\varepsilon(0)\varepsilon_0\kappa} e^{-\kappa L}. \quad [7]$$

Where κ is the inverse Debye screening length, $\varepsilon(0)$ is the static permittivity of the water solution, ε_0 is the vacuum permittivity and σ is the surface charge density of the interfaces. The Debye screening length κ^{-1} was determined as

$$\kappa^{-1} = \sqrt{\frac{\varepsilon(0)\varepsilon_0 k_B T}{2e^2 I}}, \quad [8]$$

where I is the ionic strength defined in terms of the ith ion concentration c_i and the ith ion valence z_i, as $I = \frac{1}{2}\sum_i c_i z_i^2$, and e is the elementary charge.

Although additional interactions, such as gravitational, entropic (e.g., depletion forces, osmotic pressure, etc.), and hydrophobic effects, could influence the interaction potential, previous studies (7) have shown that these contributions are negligible at separation distances around 100 nm, where stable CaSA occurs. The potential reconstruction performed in this study (see Fig. 3, using only Casimir–Lifshitz and Poisson–Boltzmann contributions) agrees with those earlier findings in the studied parameter range.

PDF. Using the experimentally determined parameters such as ionic strength I, equilibrium separation L_{eq}, surface charge density σ, and interaction area A of an individual cavity, we computed the total interaction potential as the sum of the Casimir–Lifshitz and screened electrostatic contributions. Both potentials were defined in units of eV/μm^2 and were multiplied by the interaction area A (in μm^2) to yield the total interaction energy in units of eV. To center the analysis around the equilibrium separation L_{eq}, we introduced a shifted coordinate

$$x = L - L_{\mathrm{eq}}, \quad [9]$$

such that the equilibrium position corresponds to $x = 0$. For positive displacements $x > 0$, the separation L is greater than L_{eq}, while for $x < 0$, conversely smaller. The potential was then expressed as

$$\Delta U(x) = U(x) - U(0), \quad [10]$$

which was further converted into a dimensionless form by dividing by the thermal energy $k_B T$.

The PDF was then calculated as a normalized Boltzmann distribution:

$$\mathrm{PDF}(x) = \frac{1}{Z}\cdot \exp\left(-\frac{\Delta U(x)}{k_B T}\right) \qquad \left[\frac{1}{\mathrm{nm}}\right], \quad [11]$$

where the normalization constant Z ensures that the total probability integrates to unity over the range of fluctuations ($x_{\min} - x_{\max}$):

$$Z = \int_{x_{\min}}^{x_{\max}} \exp\left(-\frac{\Delta U(x')}{k_B T}\right) dx'. \quad [12]$$

The PDF was computed in relative coordinates $x = L - L_{\mathrm{eq}}$, but shown as a function of absolute separation L.

Data, Materials, and Software Availability. All study data are included in the article and/or *SI Appendix*.

ACKNOWLEDGMENTS. We thank Dr. T. J. Antosiewicz for providing the code for the Transfer Matrix Method calculation. M.H., B.K., O.V.K., and T.O.S. acknowledge funding from the Swedish Research Council (VR project, Grant No. 2022-03347 and VR Interdisciplinary Research Environment Grant, Grant No. 2024-00545), the Knut and Alice Wallenberg Foundation (Grant No. 2019.0140), Chalmers Area of Advance Nano, and 2D-TECH VINNOVA competence Center (Ref. 2024-03852). This work was performed in part at Myfab Chalmers and the Chalmers Material Analysis Laboratory.

Author affiliations: [a]Department of Physics, Chalmers University of Technology, Göteborg 412 96, Sweden; [b]Institute of Physical Engineering, Brno University of Technology, Brno 61669, Czech Republic; and [c]Department of Chemistry, University of Illinois Urbana-Champaign, Urbana, IL 61801

Author contributions: M.H., B.K., and T.O.S. designed research; M.H., O.V.K., and B.K. performed research; M.H., O.V.K., B.K., C.J.M., and T.O.S. analyzed data; and M.H., O.V.K., B.K., C.J.M., and T.O.S. wrote the paper.

1. G. M. Whitesides, M. Boncheva, Beyond molecules: Self-assembly of mesoscopic and macroscopic components. *Proc. Natl. Acad. Sci. U.S.A.* **99**, 4769–4774 (2002).
2. Y. K. Cho, R. Wartena, S. M. Tobias, Y. M. Chiang, Self-assembling colloidal-scale devices: Selecting and using short-range surface forces between conductive solids. *Adv. Funct. Mater.* **17**, 379–389 (2007).
3. K. J. Bishop, C. E. Wilmer, S. Soh, B. A. Grzybowski, Nanoscale forces and their uses in self-assembly. *Small* **5**, 1600–1630 (2009).
4. B. V. Derjaguin, Theory of the stability of strongly charged lyophobic sol and of the adhesion of strongly charged particles in solutions of electrolytes. *Acta Phys. Chim. URSS* **14**, 633 (1941).
5. E. J. W. Verwey, Theory of the stability of lyophobic colloids. *J. Phys. Chem.* **51**, 631–636 (1947).
6. J. N. Israelachvili, *Intermolecular and Surface Forces* (Academic Press, 2011).
7. B. Munkhbat, A. Canales, B. Küçüköz, D. G. Baranov, T. O. Shegai, Tunable self-assembled Casimir microcavities and polaritons. *Nature* **597**, 214–219 (2021).
8. K. L. Young *et al.*, Assembly of reconfigurable one-dimensional colloidal superlattices due to a synergy of fundamental nanoscale forces. *Proc. Natl. Acad. Sci. U.S.A.* **109**, 2240–2245 (2012).
9. H. R. Vutukuri, S. Badaire, D. M. de Winter, A. Imhof, A. van Blaaderen, Directed self-assembly of micron-sized gold nanoplatelets into oriented flexible stacks with tunable interplate distance. *Nano Lett.* **15**, 5617–5623 (2015).
10. F. Schmidt *et al.*, Tunable critical Casimir forces counteract Casimir–Lifshitz attraction. *Nat. Phys.* **19**, 271–278 (2023).
11. M. Krasnov, A. Mazitov, N. Orekhov, D. G. Baranov, Analysis of stability and near-equilibrium dynamics of self-assembled Casimir cavities. *Phys. Rev. B* **109**, 195411 (2024).
12. V. Esteso, D. Frustaglia, S. Carretero-Palacios, H. Míguez, Casimir–Lifshitz optical resonators: A new platform for exploring physics at the nanoscale. *Adv. Phys. Res.* **3**, 2300065 (2024).
13. D. Samanta, R. Klajn, Aqueous light-controlled self-assembly of nanoparticles. *Adv. Opt. Mater.* **4**, 793–800 (2016).

14. H. B. Casimir, On the attraction between two perfectly conducting plates. *Proc. Kon. Ned. Akad. Wet.* **51**, 793 (1948).
15. E. M. Lifshitz, "The theory of molecular attractive forces between solids" in *Perspectives in Theoretical Physics*, L. P. Pitaevskii, Ed. (Elsevier, 1992), pp. 329–349.
16. I. E. Dzyaloshinskii, E. M. Lifshitz, L. P. Pitaevskii, The general theory of van der Waals forces. *Adv. Phys.* **10**, 165–209 (1961).
17. D. A. Somers, J. L. Garrett, K. J. Palm, J. N. Munday, Measurement of the Casimir torque. *Nature* **564**, 386–389 (2018).
18. B. Küçüköz *et al*., Quantum trapping and rotational self-alignment in triangular Casimir microcavities. *Sci. Adv.* **10**, eadn1825 (2024).
19. G. Wang *et al*., Nanoalignment by critical Casimir torques. *Nat. Commun.* **15**, 5086 (2024).
20. H. Chan, V. Aksyuk, R. Kleiman, D. Bishop, F. Capasso, Nonlinear micromechanical Casimir oscillator. *Phys. Rev. Lett.* **87**, 211801 (2001).
21. J. N. Munday, F. Capasso, V. A. Parsegian, Measured long-range repulsive Casimir–Lifshitz forces. *Nature* **457**, 170–173 (2009).
22. J. N. Munday, F. Capasso, Repulsive Casimir and van der Waals forces: From measurements to future technologies. *Int. J. Mod. Phys. A* **25**, 2252–2259 (2010).
23. R. Zhao *et al*., Stable Casimir equilibria and quantum trapping. *Science* **364**, 984–987 (2019).
24. V. Esteso, S. Carretero-Palacios, H. Míguez, Casimir–Lifshitz force based optical resonators. *J. Phys. Chem. Lett.* **10**, 5856–5860 (2019).
25. A. N. Babar *et al*., Self-assembled photonic cavities with atomic-scale confinement. *Nature* **624**, 57–63 (2023).
26. H. B. Chan, V. A. Aksyuk, R. N. Kleiman, D. J. Bishop, F. Capasso, Quantum mechanical actuation of microelectromechanical systems by the Casimir force. *Science* **291**, 1941–1944 (2001).
27. M. Imboden, J. Morrison, D. Campbell, D. Bishop, Design of a Casimir-driven parametric amplifier. *J. Appl. Phys.* **116** (2014).
28. B. Spreng *et al*., Universal Casimir attraction between filaments at the cell scale. *New J. Phys.* **26**, 013009 (2024).
29. G. Klimchitskaya, U. Mohideen, V. Mostepanenko, The Casimir force between real materials: Experiment and theory. *Rev. Mod. Phys.* **81**, 1827 (2009).
30. A. W. Rodriguez *et al*., Designing evanescent optical interactions to control the expression of Casimir forces in optomechanical structures. *Appl. Phys. Lett.* **98** (2011).
31. R. Decca *et al*., Tests of new physics from precise measurements of the Casimir pressure between two gold-coated plates. *Phys. Rev. D* **75**, 077101 (2007).
32. C. N. Lunardi, A. J. Gomes, F. S. Rocha, J. De Tommaso, G. S. Patience, Experimental methods in chemical engineering: Zeta potential. *Can. J. Chem. Eng.* **99**, 627–639 (2021).
33. A. H. Jalil, U. Pyell, Quantification of zeta-potential and electrokinetic surface charge density for colloidal silica nanoparticles dependent on type and concentration of the counterion: Probing the outer Helmholtz plane. *J. Phys. Chem. C* **122**, 4437–4453 (2018).
34. S. Chen *et al*., Rapid seedless synthesis of gold nanoplates with microscaled edge length in a high yield and their application in SERS. *Nano-Micro Lett.* **8**, 328–335 (2016).
35. J. Vivek, I. J. Burgess, Quaternary ammonium bromide surfactant adsorption on low-index surfaces of gold. 1. Au (111). *Langmuir* **28**, 5031–5039 (2012).
36. P. J. Scales, F. Grieser, T. W. Healy, L. J. Magid, Electrokinetics of muscovite mica in the presence of adsorbed cationic surfactants. *Langmuir* **8**, 277–282 (1992).
37. R. J. Hunter, *Introduction to Modern Colloid Science* (Oxford University Press, 1993).
38. S. B. Johnson, C. J. Drummond, P. J. Scales, S. Nishimura, Comparison of techniques for measuring the electrical double layer properties of surfaces in aqueous solution: Hexadecyltrimethylammonium bromide self-assembly structures as a model system. *Langmuir* **11**, 2367–2375 (1995).
39. R. Prathapan, R. Thapa, G. Garnier, R. F. Tabor, Modulating the zeta potential of cellulose nanocrystals using salts and surfactants. *Colloids Surf. A: Physicochem. Eng. Asp.* **509**, 11–18 (2016).
40. A. Gupta, S. Vasudevan, Understanding surfactant stabilization of MoS_2 nanosheets in aqueous dispersions from zeta potential measurements and molecular dynamics simulations. *J. Phys. Chem. C* **122**, 19243–19250 (2018).
41. E. L. Correia, S. Thakur, A. Ervin, E. Shields, S. Razavi, Adsorption of surfactant molecules onto the surface of colloidal particles: Case of like-charged species. *Colloids Surf. A: Physicochem. Eng. Asp.* **676**, 132142(2023).
42. D. C. Grahame, The electrical double layer and the theory of electrocapillarity. *Chem. Rev.* **41**, 441–501 (1947).
43. D. Chen *et al*., Nonlinear dependence (on ionic strength, pH) of surface charge density and zeta potential in microchannel electrokinetic flow. *Heliyon* **9**, e20888 (2023).
44. D. C. Prieve, N. A. Frej, Total internal reflection microscopy: A quantitative tool for the measurement of colloidal forces. *Langmuir* **6**, 396–403 (1990).
45. H. Shen *et al*., Single particle tracking: From theory to biophysical applications. *Chem. Rev.* **117**, 7331–7376 (2017).
46. M. Fränzl, F. Cichos, Hydrodynamic manipulation of nano-objects by optically induced thermo-osmotic flows. *Nat. Commun.* **13**, 656 (2022).
47. J. Kim, O. J. Martin, Probing surfactant bilayer interactions by tracking optically trapped single nanoparticles. *Adv. Mater. Interfaces* **10**, 2201793 (2023).
48. M. A. Bevan, D. C. Prieve, Direct measurement of retarded van der Waals attraction. *Langmuir* **15**, 7925–7936 (1999).
49. J. Israelachvili, Direct measurements of forces between surfaces in liquids at the molecular level. *Proc. Natl. Acad. Sci. U.S.A.* **84**, 4722–4724 (1987).
50. W. A. Ducker, T. J. Senden, R. M. Pashley, Direct measurement of colloidal forces using an atomic force microscope. *Nature* **353**, 239–241 (1991).
51. H. J. Butt, Measuring electrostatic, van der Waals, and hydration forces in electrolyte solutions with an atomic force microscope. *Biophys. J.* **60**, 1438–1444 (1991).
52. J. P. Cleveland, T. Schäffer, P. K. Hansma, Probing oscillatory hydration potentials using thermal–mechanical noise in an atomic-force microscope. *Phys. Rev. B* **52**, R8692 (1995).
53. O. H. Willemsen, L. Kuipers, K. O. van der Werf, B. G. de Grooth, J. Greve, Reconstruction of the tip-surface interaction potential by analysis of the Brownian motion of an atomic force microscope tip. *Langmuir* **16**, 4339–4347 (2000).
54. Á. V. Delgado, F. González-Caballero, R. Hunter, L. Koopal, J. Lyklema, Measurement and interpretation of electrokinetic phenomena. *J. Colloid Interface Sci.* **309**, 194–224 (2007).
55. S. Bhattacharjee, DLS and zeta potential–What they are and what they are not? *J. Control. Release* **235**, 337–351 (2016).
56. H. J. Butt, M. Kappl, *Surface and Interfacial Forces* (John Wiley & Sons, 2018).
57. L. B. Pires *et al*., Probing the screening of the Casimir interaction with optical tweezers. *Phys. Rev. Res.* **3**, 033037 (2021).
58. R. R. Kumal, T. E. Karam, L. H. Haber, Determination of the surface charge density of colloidal gold nanoparticles using second harmonic generation. *J. Phys. Chem. C* **119**, 16200–16207 (2015).
59. R. Li *et al*., Study on the assembly structure variation of cetyltrimethylammonium bromide on the surface of gold nanoparticles. *ACS Omega* **5**, 4943–4952 (2020).
60. Y. Liu, M. Tourbin, S. Lachaize, P. Guiraud, Silica nanoparticles separation from water: Aggregation by cetyltrimethylammonium bromide (CTAB). *Chemosphere* **92**, 681–687 (2013).
61. A. N. Laguta *et al*., Interaction of aqueous suspensions of single-walled oxidized carbon nanotubes with inorganic and organic electrolytes. *J. Mol. Liq.* **347**, 117948 (2022).
62. M. Khademi, W. Wang, W. Reitinger, D. P. Barz, Zeta potential of poly (methyl methacrylate) (PMMA) in contact with aqueous electrolyte-surfactant solutions. *Langmuir* **33**, 10473–10482 (2017).
63. J. Kim, O. J. Martin, Surfactants control optical trapping near a glass wall. *J. Phys. Chem. C* **126**, 378–386 (2021).
64. M. A. Sobhan, M. J. Withford, E. M. Goldys, Enhanced stability of gold colloids produced by femtosecond laser synthesis in aqueous solution of CTAB. *Langmuir* **26**, 3156–3159 (2010).
65. C. A. Başar, A. Karagunduz, B. Keskinler, A. Cakici, Effect of presence of ions on surface characteristics of surfactant modified powdered activated carbon (PAC). *Appl. Surf. Sci.* **218**, 170–175 (2003).
66. T. K. Sau, C. J. Murphy, Self-assembly patterns formed upon solvent evaporation of aqueous cetyltrimethylammonium bromide-coated gold nanoparticles of various shapes. *Langmuir* **21**, 2923–2929 (2005).
67. A. Lambrecht, P. A. M. Neto, S. Reynaud, The Casimir effect within scattering theory. *New J. Phys.* **8**, 243 (2006).